Supporting Information for "Aseismic Fault Slip during a Shallow Normal-Faulting Seismic Swarm Constrained Using a Physically-Informed Geodetic Inversion Method"

Yu Jiang[1], Sergey V. Samsonov[2], and Pablo J. González[1,3]

[1]COMET, Dept. Earth, Ocean and Ecological Sciences, School of Environmental Sciences, University of Liverpool, Liverpool, L69 3BX, United Kingdom.

[2]Canada centre for Mapping and Earth Observation, Natural Resources Canada, 560 Rochester Street, Ottawa, ON K1S5K2, Canada.

[3]Department of Life and Earth Sciences, Instituto de Productos Naturales y Agrobiología (IPNA-CSIC), 38206 La Laguna, Tenerife, Canary Islands, Spain.

Contents of this file

1. Figures S1 to S10

2. Tables S1

Introduction This document contains supplementary figures and table. Figure S1 shows the observed and modelled InSAR phase for the synthetic case 1. Figures S2-S3 show the observed and modelled InSAR phase for synthetic case 2 (pulse-like ruptures). Figure S4-S5 show the observed and modelled InSAR phase for synthetic case 2 (crack-like ruptures). Figure S6 shows the wrapped and unwrapped InSAR phase for the descending ENVISAT

interferogram. Figure S7 shows the estimation of the covariance function from the non-deformed region. Figure S8 shows the inversion for two subfaults in the 2011 Hawthorne swarm, including the southern subfault in the pre-M4.6 stage, and the northern subfault during the co- and post-M4.6 stage. Figure S9 shows the modelled InSAR phases based on the fault geometry from nonlinear inversion (WGBIS). Figure S10 shows the degree of similarity between idealised one-ellipse crack model and published finite slip distribution datasets as a function of magnitudes. Table S1 summarised the parameters of slow slip listed in Section 5.2. For each event the table lists the event location, date, type and the reference from which the information was obtained.

References

Bletery, Q., & Nocquet, J. M. (2020). Slip bursts during coalescence of slow slip events in Cascadia. *Nature Communications*, *11*(1), 1–6. doi: 10.1038/s41467-020-15494-4

Cheloni, D., D'Agostino, N., Selvaggi, G., Avallone, A., Fornaro, G., Giuliani, R., ... Tizzani, P. (2017). Aseismic transient during the 2010-2014 seismic swarm: Evidence for longer recurrence of M≥6.5 earthquakes in the Pollino gap (Southern Italy)? *Scientific Reports*, *7*(1), 1–10. doi: 10.1038/s41598-017-00649-z

De Barros, L., Cappa, F., Deschamps, A., & Dublanchet, P. (2020). Imbricated Aseismic Slip and Fluid Diffusion Drive a Seismic Swarm in the Corinth Gulf, Greece. *Geophysical Research Letters*, *47*(9). doi: 10.1029/2020GL087142

Guglielmi, Y., Cappa, F., Avouac, J. P., Henry, P., & Elsworth, D. (2015). Seismicity triggered by fluid injection-induced aseismic slip. *Science*, *348*(6240), 1224–1226. doi: 10.1126/science.aab0476

Hirose, H., & Obara, K. (2010). Recurrence behavior of short-term slow slip and corre-

lated nonvolcanic tremor episodes in western Shikoku, southwest Japan. *Journal of Geophysical Research: Solid Earth*, *115*(B6), 0–21. doi: 10.1029/2008JB006050

Houston, H., Delbridge, B. G., Wech, A. G., & Creager, K. C. (2011). Rapid tremor reversals in Cascadia generated by a weakened plate interface. *Nature Geoscience*, *4*(6), 404–409. doi: 10.1038/ngeo1157

Hussain, E., Hooper, A., Wright, T. J., Walters, R. J., & Bekaert, D. P. (2016). Interseismic strain accumulation across the central North Anatolian Fault from iteratively unwrapped InSAR measurements. *Journal of Geophysical Research: Solid Earth*, *121*(12), 9000–9019. doi: 10.1002/2016JB013108

Jiang, Y., & González, P. J. (2020). Bayesian Inversion of Wrapped Satellite Interferometric Phase to Estimate Fault and Volcano Surface Ground Deformation Models. *Journal of Geophysical Research: Solid Earth*, *125*(5). doi: 10.1029/2019JB018313

Johanson, I. A., & Bürgmann, R. (2005). Creep and quakes on the northern transition zone of the San Andreas fault from GPS and InSAR data. *Geophysical Research Letters*, *32*(14), 1–5. doi: 10.1029/2005GL023150

Jolivet, R., Lasserre, C., Doin, M. P., Guillaso, S., Peltzer, G., Dailu, R., ... Xu, X. (2012). Shallow creep on the Haiyuan Fault (Gansu, China) revealed by SAR Interferometry. *Journal of Geophysical Research: Solid Earth*, *117*(B6), 6401. doi: 10.1029/2011JB008732

Khoshmanesh, M., Shirzaei, M., & Nadeau, R. M. (2015). Time-dependent model of aseismic slip on the central San Andreas Fault from InSAR time series and repeating earthquakes. *Journal of Geophysical Research: Solid Earth*, *120*(9), 6658–6679. doi: 10.1002/2015JB012039

Kyriakopoulos, C., Chini, M., Bignami, C., Stramondo, S., Ganas, A., Kolligri, M., & Moshou, A. (2013). Monthly migration of a tectonic seismic swarm detected by DInSAR: Southwest Peloponnese, Greece. *Geophysical Journal International*, *194*(3), 1302–1309. doi: 10.1093/gji/ggt196

López-Comino, J. A., Stich, D., Morales, J., & Ferreira, A. M. (2016). Resolution of rupture directivity in weak events: 1-D versus 2-D source parameterizations for the 2011, Mw 4.6 and 5.2 Lorca earthquakes, Spain. *Journal of Geophysical Research: Solid Earth*, *121*(9), 6608–6626. doi: 10.1002/2016JB013227

Mesimeri, M., & Karakostas, V. (2018). Repeating earthquakes in western Corinth Gulf (Greece): Implications for aseismic slip near locked faults. *Geophysical Journal International*, *215*(1), 659–676. doi: 10.1093/gji/ggy301

Nadeau, R. M., & McEvilly, T. V. (1999). Fault slip rates at depth from recurrence intervals of repeating microearthquakes. *Science*, *285*(5428), 718–721. doi: 10.1126/science.285.5428.718

Ozawa, S., Yarai, H., & Kobayashi, T. (2019). Recovery of the recurrence interval of Boso slow slip events in Japan. *Earth, Planets and Space*, *71*(1), 1–8. doi: 10.1186/s40623-019-1058-y

Passarelli, L., Rivalta, E., Jónsson, S., Hensch, M., Metzger, S., Jakobsdóttir, S. S., ... Dahm, T. (2018). Scaling and spatial complementarity of tectonic earthquake swarms. *Earth and Planetary Science Letters*, *482*, 62–70. doi: 10.1016/j.epsl.2017.10.052

Radiguet, M., Cotton, F., Vergnolle, M., Campillo, M., Valette, B., Kostoglodov, V., & Cotte, N. (2011). Spatial and temporal evolution of a long term slow slip event: the

2006 Guerrero Slow Slip Event. *Geophysical Journal International*, *184*(2), 816–828. doi: 10.1111/j.1365-246X.2010.04866.x

Rousset, B., Fu, Y., Bartlow, N., & Bürgmann, R. (2019). Weeks-Long and Years-Long Slow Slip and Tectonic Tremor Episodes on the South Central Alaska Megathrust. *Journal of Geophysical Research: Solid Earth*, *124*(12), 13392–13403. doi: 10.1029/2019JB018724

Schmidt, D. A., Bürgmann, R., Nadeau, R. M., & D'Alessio, M. (2005). Distribution of aseismic slip rate on the Hayward fault inferred from seismic and geodetic data. *Journal of Geophysical Research: Solid Earth*, *110*(B8), 1–15. doi: 10.1029/2004JB003397

Scott, C., Bunds, M., Shirzaei, M., & Toke, N. (2020). Creep Along the Central San Andreas Fault From Surface Fractures, Topographic Differencing, and InSAR. *Journal of Geophysical Research: Solid Earth*, *125*(10), e2020JB019762. doi: 10.1029/2020JB019762

Song, X., Jiang, Y., Shan, X., Gong, W., & Qu, C. (2019). A Fine Velocity and Strain Rate Field of Present-Day Crustal Motion of the Northeastern Tibetan Plateau Inverted Jointly by InSAR and GPS. *Remote Sensing 2019, Vol. 11, Page 435*, *11*(4), 435. doi: 10.3390/RS11040435

Turner, R. C., Nadeau, R. M., & Bürgmann, R. (2013). Aseismic slip and fault interaction from repeating earthquakes in the Loma Prieta aftershock zone. *Geophysical Research Letters*, *40*(6), 1079–1083. doi: 10.1002/grl.50212

Wech, A. G., Creager, K. C., & Melbourne, T. I. (2009). Seismic and geodetic constraints on Cascadia slow slip. *Journal of Geophysical Research: Solid Earth*, *114*(10). doi:

10.1029/2008JB006090

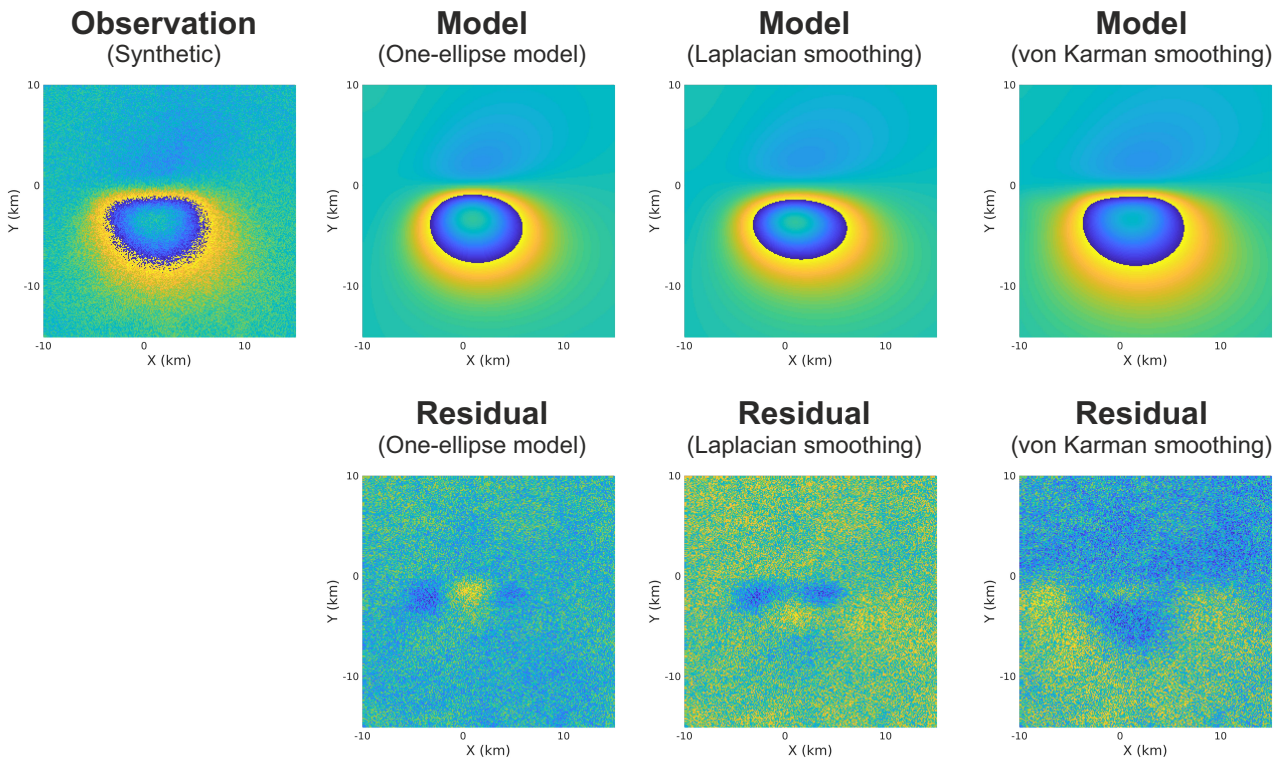

Figure S1. Synthetic and modelled InSAR phases for a synthetic case. The observed InSAR phase is forward calculated on the basis of the synthetic fault slip in Figure 2(a). The modelled InSAR phases are forward calculated on the basis of modelled slip distributions in Figure 2(b)-(c) estimated by the one-ellipse model and the laplacian smoothing. The bottom images show the residual phases.

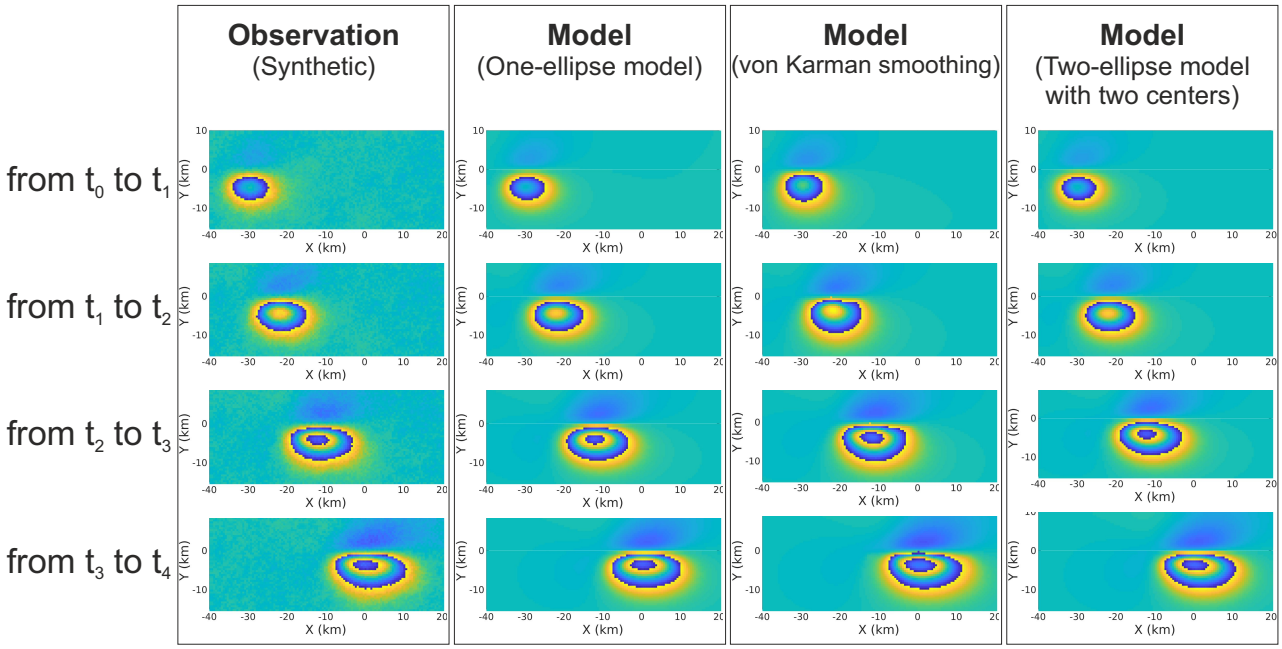

Figure S2. Synthetic and modelled InSAR phases for synthetic case 2 (pulse-like ruptures). The observed InSAR phase is forward calculated on the basis of the synthetic fault slip in Figure 3(a). The modelled InSAR phases are forward calculated on the basis of modelled slip distributions in Figure 3(b)-(d) with various methods: the one-ellipse model, the von Karman smoothing, and the two-ellipse model with different centres.

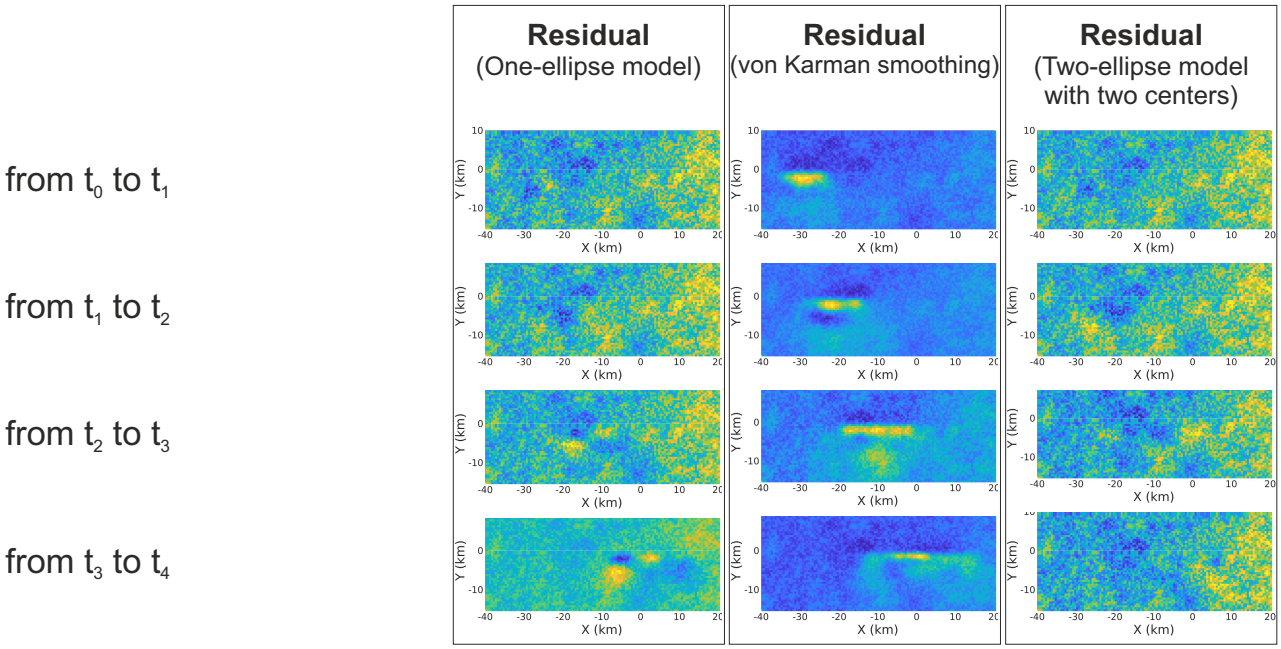

Figure S3. Residual InSAR phases for synthetic case 2 (pulse-like ruptures).

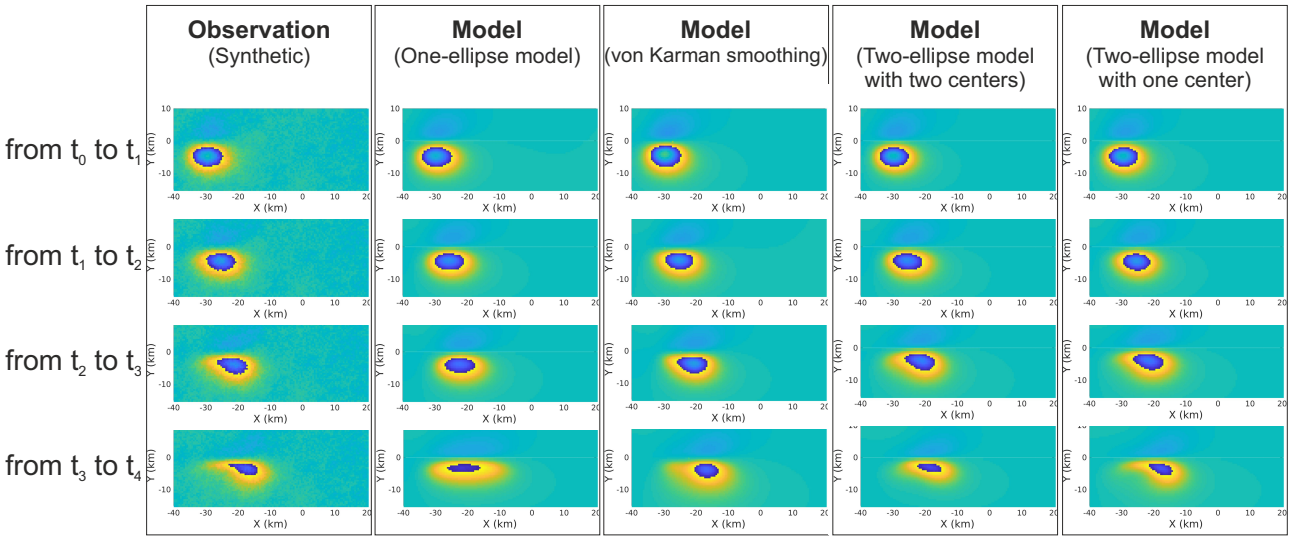

Figure S4. Synthetic and modelled InSAR phases for synthetic case 2 (crack-like ruptures). The observed InSAR phase is forward calculated on the basis of the synthetic fault slip in Figure 4(a). The modelled InSAR phases are forward calculated on the basis of modelled slip distributions in Figure 4(b)-(e) with various methods: the one-ellipse model, the von Karman smoothing, and the two-ellipse model with different centres and with the same centre.

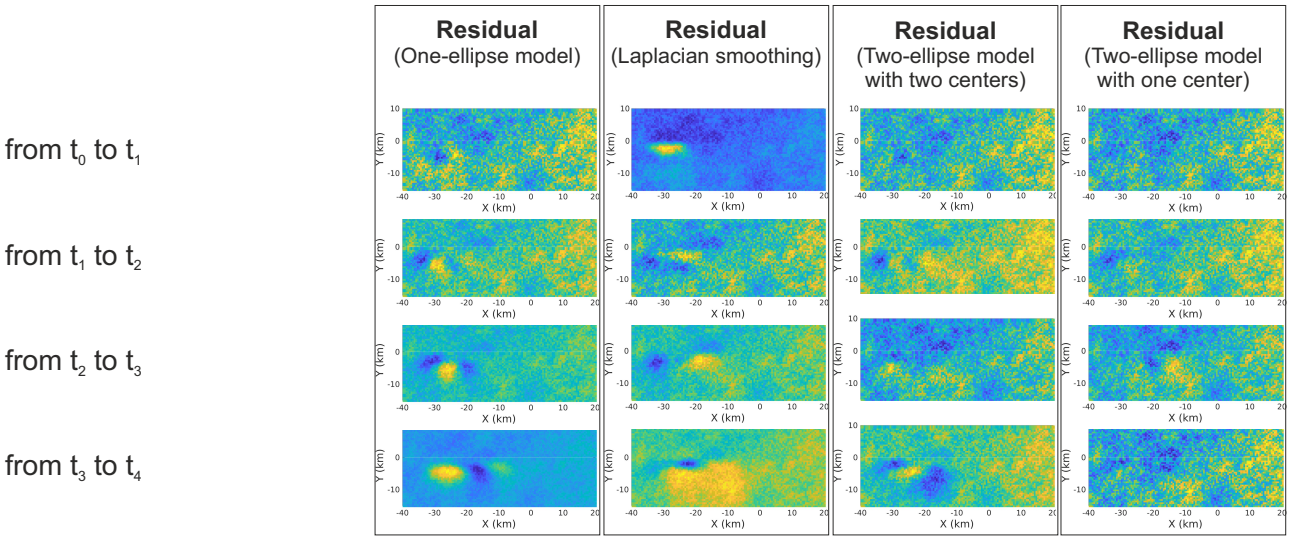

Figure S5. Residual InSAR phases for synthetic case 2 (crack-like ruptures).

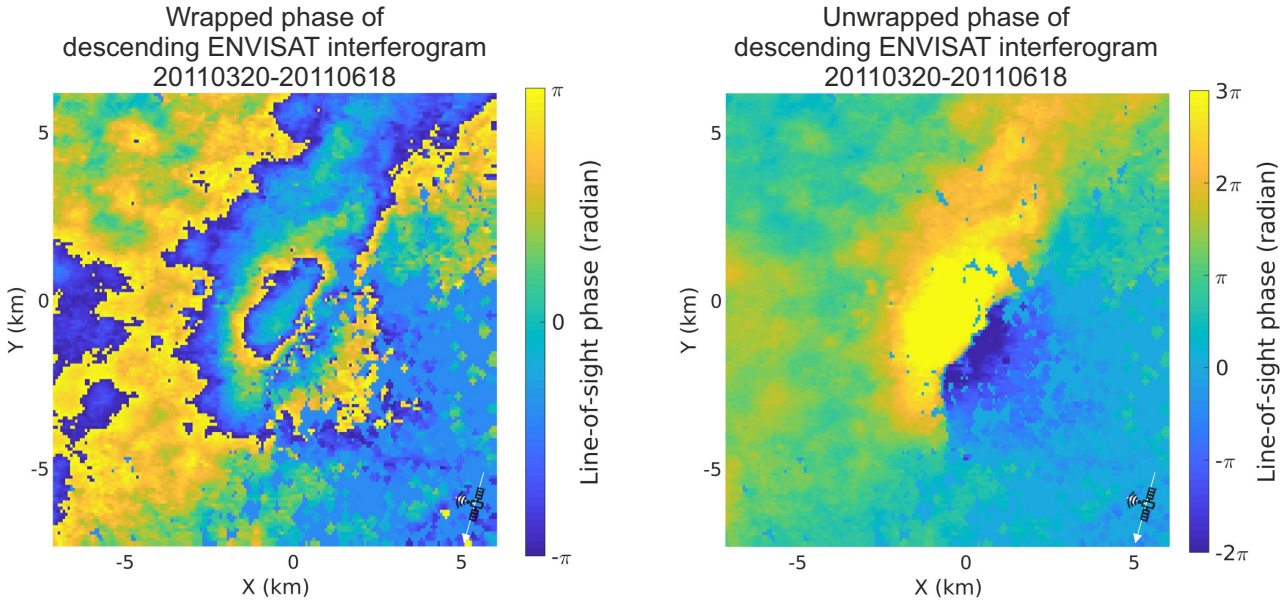

Figure S6. Wrapped and unwrapped phase in the descending ENVISAT interferogram 2011/03/20-2011/06/18.

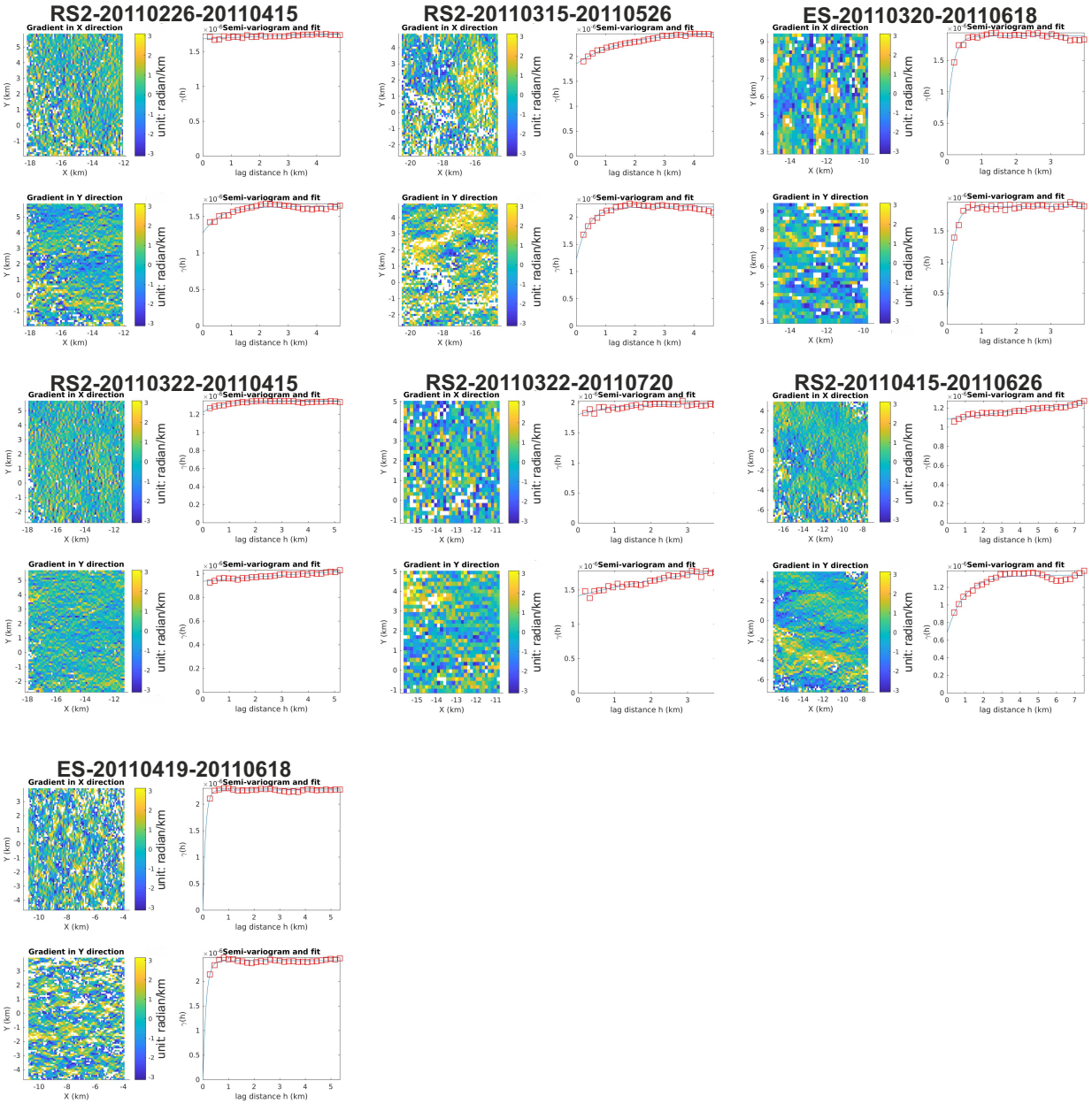

Figure S7. Covariance function estimation from the phase in the nondeformed region of the interferograms used in the 2011 Hawthorne seismic swarm. The chosen region for covariance estimation is the undeformed region. For each panel, images on the left are the downsampled phase gradients in X-direction and Y-direction; images on the right side show the experimental (rectangular) and theoretical (solid line) semivariograms are shown for phase gradients in X-direction and Y-direction, estimating from the downsampled phase gradients according to equation 9 in Jiang and González (2020).

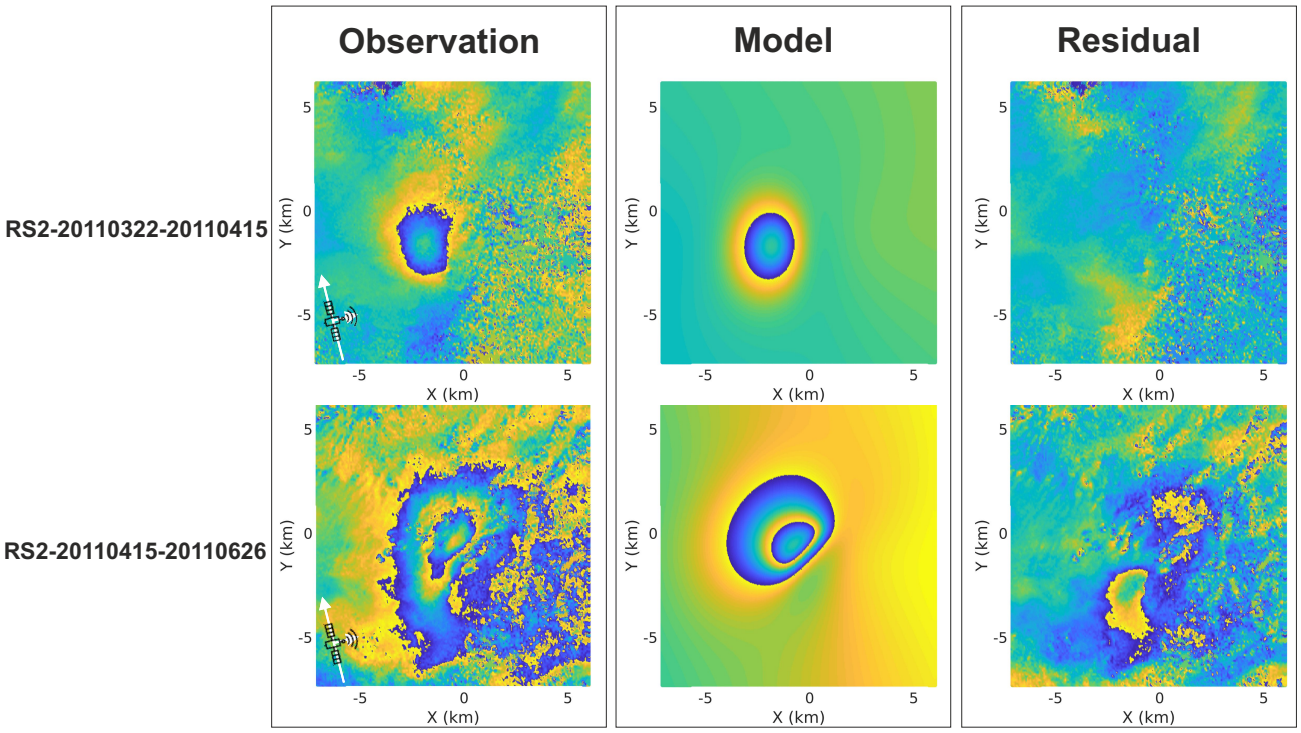

Figure S8. Observed and modelled InSAR displacements with WGBIS. Images at the top row show the observed, modelled and residual phases for ascending RADARSAT-2 interferogram 2011/03/22-2011/04/15, covering the pre-M4.6 stage of the 2011 Hawthorne swarm. Images at the bottom row show the observed, modelled and residual phases for ascending RADARSAT-2 interferogram 2011/04/15-2011/06/26, covering the co- and post-M4.6 stage of the 2011 Hawthorne swarm.

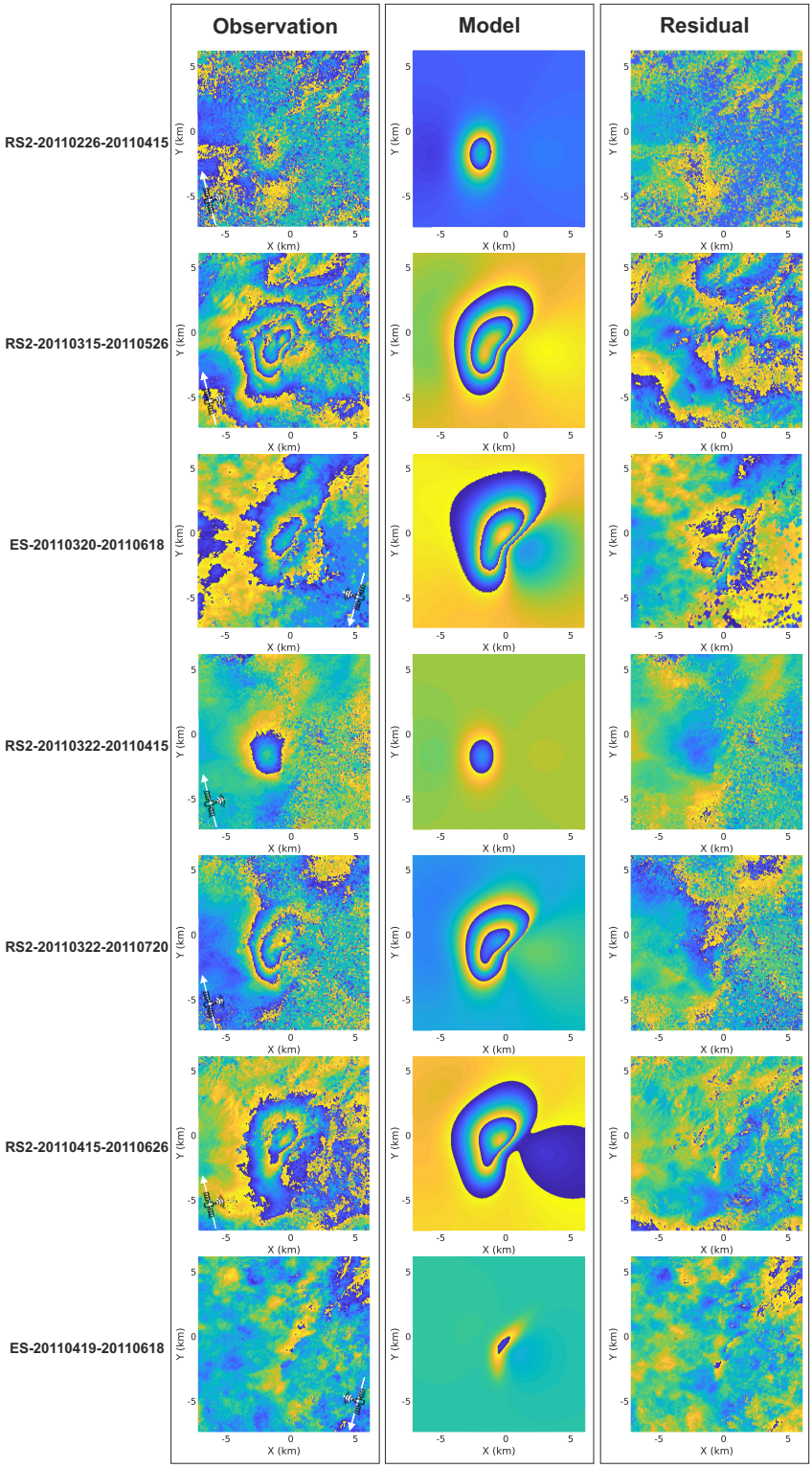

Figure S9. Observed and modelled InSAR displacements of the 2011 Hawthorne swarm by using the discretized fault geometry retrieved from WGBIS. The modelled phases are forward calculated on the basis of the modelled slip distributions in Figure 8(a) and discretized fault geometry in Figure 7(d).

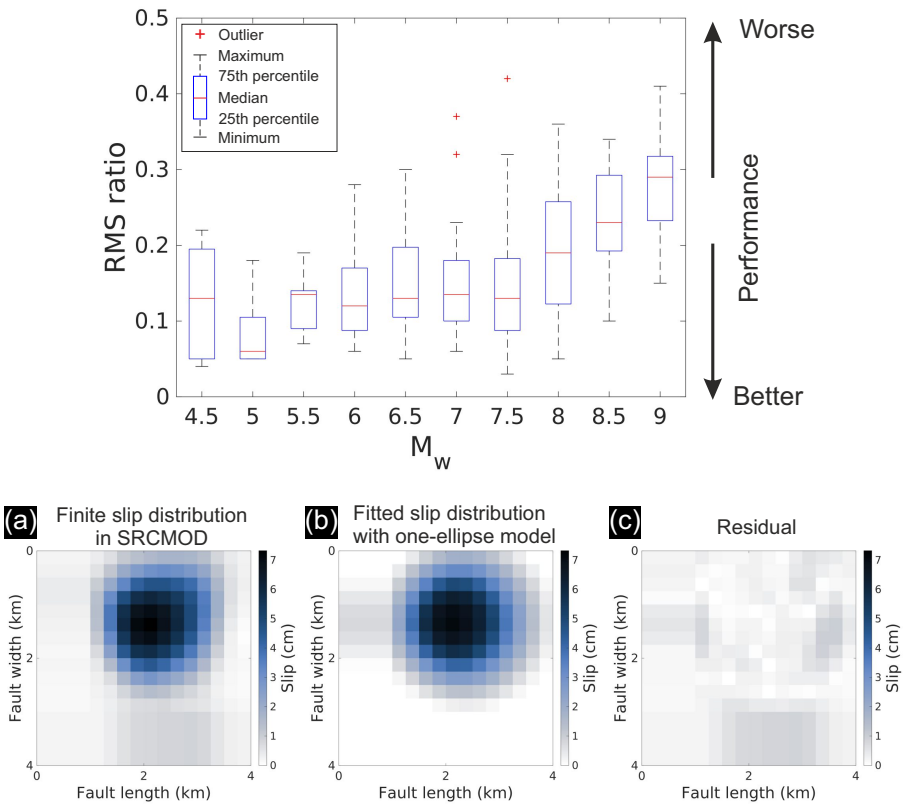

Figure S10. This figure shows the degree of similarity between idealised one-ellipse crack model and published finite slip distribution datasets as a function of magnitudes. A one-ellipse crack model is used to approximate the finite slip distributions in SRCMOD for each dataset containing 25 fault patches or more. We obtain a best fitting model for each selected dataset. We estimate the misfit between the best fitting crack model and SRCMOD estimated fault slips as the RMSE. Top image presents the ratio between RMSE and peak slip for each case in the SRCMOD dataset. Lower values of the ratio indicate better agreement. Bottom images present an example for comparison of a SRCMOD event (2011 M_w 4.6 Lorca earthquakes, Spain, López-Comino et al. (2016)) and its best-fitting ellipse model.

Table S1. Parameters of slow slip phenomena considered in this study

Name	Type	Value	Source location and date	(Reference)
Peak slip rate (cm/day)	SSE	0.27	[124°W, 49°N], Cascadia subduction zone, 2013	(Bletery & Nocquet, 2020)
		0.3	[149°W, 62°N], Central Alaska Megathrust, 2010	(Rousset et al., 2019)
		0.6-1.1	[132.5°E, 33.5°N], Western Shikoku, Japan, 2002-2007	(Hirose & Obara, 2010)
		1.1-2.8	[141°E, 35°N], Boso peninsula, Japan, 1996-2018	(Ozawa et al., 2019)
	Seismic swarm	0.26	[22°E, 37.24°N], Peloponnese peninsula, Greece, 2011	(Kyriakopoulos et al., 2013)
	Fluid injection experiments	35	France, ?	(Guglielmi et al., 2015)
	Fault creep	0.001	[122.25°W, 37.5°N], Hayward fault, USA, 1992-2000	(Schmidt et al., 2005)
		0.001	[105°E, 36.5°N], Haiyuan fault, China, 2003-2010	(Jolivet et al., 2012); (Song et al., 2019)
		0.002	[32.5°E, 40.75°N], North Anatolia fault, Turkey, 2003-2010	(Hussain et al., 2016)
		0.005	[121.4°W, 36.8°N], San Anreas fault, USA, 2001-2003	(Johanson & Bürgmann, 2005)
		0.008	[121°W, 36.2°N], Central segment of San Andreas fault, USA, 2003-2011	(Khoshmanesh et al., 2015)
		0.007	[121°W, 36.4°N], Central segment of San Andreas fault, USA, 2012-2020	(Scott et al., 2020)
Average rate of slip increment (cm/day)	SSE	0.03-0.14	[100°W, 18°N], Mexican subduction zone, 2006	(Radiguet et al., 2011)
	Seismic swarm	0.1	[16°E, 39.9°N], Pollino gap, Southern Italy, 2010-2014	(Cheloni et al., 2017)
	Repeating earthquakes	0.01	[116.7°W, 36.7°N], San Andreas fault, USA, 1994	(Nadeau & McEvilly, 1999)
		0.003	[121.6°W, 36.8°N], San Anreas fault, USA, 2003-2006	(Turner et al., 2013)
		0.0006	[22°E, 38.4°N], Corinth Gulf, Greece, 2008-2014	(Mesimeri & Karakostas, 2018)
Migration velocity (km/day)	SSE	∼10	[132.5°E, 33.5°N], Western Shikoku, Japan, 2002-2007	(Hirose & Obara, 2010)
	ETS	∼10	[123.5°W, 48.5°N], Cascadia subduction zone, 2004-2008	(Wech et al., 2009)
	RTR	160-400	[123°W, 48°N], Cascadia subduction zone, 2004-2009	(Houston et al., 2011)
	Seismic swarm	0.5-14	[18.6°W, 66.3°N], North Iceland, 1997-2015	(Passarelli et al., 2018)
		2-10	[22°E, 38.4°N], Corinth Gulf, Greece, 2015	(De Barros et al., 2020)